



## Studies of synergy between metal–support interfaces and selective hydrogenation of HMF to DMF in water



Reena Goyal<sup>a</sup>, Bipul Sarkar<sup>a</sup>, Arijit Bag<sup>b</sup>, Nazia Siddiqui<sup>a</sup>, Deepa Dumbre<sup>c</sup>, Nishita Lucas<sup>d</sup>, Suresh Kumar Bhargava<sup>c</sup>, Ankur Bordoloi<sup>a,\*</sup>

<sup>a</sup>Nano Catalysis Area, Refinery Technology Division, CSIR–Indian Institute of Petroleum, Dehradun 248005, India

<sup>b</sup>Chemical Science Division, IISER Kolkata, Mohanpur, Nadia, West Bengal, India

<sup>c</sup>Applied Sciences, Science, Engineering and Health, RMIT, Melbourne, Australia

<sup>d</sup>Catalysis Division, CSIR–National Chemical Laboratory, Pune, India

### ARTICLE INFO

#### Article history:

Received 30 March 2016

Revised 13 May 2016

Accepted 16 May 2016

#### Keywords:

Biofuels

Biomass

Hydrogenation

Mesoporous carbon

Ni–CN<sub>x</sub>

### ABSTRACT

Metal–support interfaces play a very important role in heterogeneous catalysis. The interfacial interactions not only are responsible for stabilizing the necessary oxidation state to facilitate the reaction but also enhance the stability of the catalyst system. Nano dispersion of Ni on mesoporous nitrogen-rich carbon material has been achieved using two different synthesis methods. It was observed that nickel (0) gets stabilized by strong interfacial interaction with the nitrogen atoms of the support material, and the material was found to be very economic and efficient for the conversion of HMF to DMF in aqueous medium. The material shows  $\geq 99\%$  conversion to 5-(hydroxymethyl) furfural (HMF) within 6 h of reaction with 98.7% DMF selectivity. A unique correlation between synthesis methods and particle sizes with catalytic performance has been observed for these newly developed materials. Furthermore, a DFT calculation has been performed to predict the reaction mechanism.

© 2016 Elsevier Inc. All rights reserved.

### 1. Introduction

The growing interest in finding renewable feedstock for fuel and chemicals to replace the conventional resources leaves us multiple options. The bioderived feedstocks are one of the major contenders in this race [1,2]. In recent years, the scientific and industrial communities have been oriented toward the reductive upgrading of biomass-derived molecules for the sustainable production of feedstocks for the chemical industry and the transportation sector [3]. Total biomass production via photosynthesis is 200 billion metric tons, which contain  $3 \times 10^{18}$  kJ energy per year, 10 times of the present annual energy consumption of world [4]. Bioethanol is the only liquid fuel that is produced commercially adjacent to the sugar industry or from oilseeds [5]. However, the obstructions to this process are land requirements for food production and other purposes. It has been observed that first generation bioethanol production does not meet the demand for oil-based economic growth or substitute for fossil fuel [6]. The most effective pathway is pre-treatment of biomass-derived lignocellulose, selective separation of its three components, and selective transformation of this

component for the production of second generation biofuel [7]. With the recent boom in transportation sectors, biomass-based biofuels are viewed as potential participants, as they provide a renewable carbon source for transportation fuels and chemicals [8]. In this respect, 5-(hydroxymethyl) furfural (HMF) obtained from the dehydration of sugars is an excellent platform for bio-based fuels [9–11].

The selective hydrogenolysis of HMF to 2,5-dimethylfuran (DMF) exhibits great potential for the production of oil-based fuel substitutes from renewable energy sources [12]. However, selective production of DMF from HMF hydrogenolysis using non-noble-metal catalysts is still a challenge. For selective hydrogenation to DMF, hydrogen has to reduce formyl and hydroxyl groups without affecting the furan ring. DMF exhibits higher energy density (31.5 MJ/L), higher research octane number (119), and lower volatility (boiling point 92–94 °C) with a lower energy separation characteristic than market leading ethanol [13]. All these properties make DMF a more excellent, appropriate and promising bio-derived liquid fuel [14]. Another promising property of DMF is it can be used as a fuel additive to boost research octane number (RON) [15].

The standard catalyst system date for hydrogenolysis of HMF to DMF is mainly CuRu/carbon- and PtCo@HCS-based bimetallic

\* Corresponding author. Fax: +91 135 2660202.

E-mail address: [ankurb@iip.res.in](mailto:ankurb@iip.res.in) (A. Bordoloi).

catalysts. CuRu/C gives 100% HMF conversion with 61% DMF selectivity [16] and Pt Co@HCS gives 100% conversion with 98% DMF yield at 180 °C in 2 h. [17] An electrocatalyst strategy has also been explored by Nilges and Schroder at room temperature and atmospheric pressure for hydrogenation of HMF into DMF [18]. Recently, nickel hydrotalcite has been reported for the hydrogenation of HMF [19]. It is quite well known that characteristics of the support play an important role in determining the catalytic activity of materials [20]. Noble metals such as Pd, Pt, and Ru supported on carbon prove to be excellent catalysts for hydrogenation of biomass-derived chemicals [21–24]. The main shortcoming of this material is leaching of metal nanoparticles during catalysis, which is mostly due to less interfacial interaction between the support and the metal nanoparticles. Hence, modification of carbon material by any heteroatom doping can enhance the interaction between the support and the metal nanoparticles. For example, incorporation of nitrogen into the surface results in increased conductivity, polarity, and basicity due to the electron-donating effect of the heteroatom. Therefore, nitrogen-doped carbon materials are expected to be suitable supports for metal catalysts, as the nitrogen atoms not only can provide strong bonding to the metal, but also behave as electron donors [25–27]. Moreover, metal nanoclusters are very interesting materials due to their high conductivity, good biocompatibility, and low cost, which makes them attractive for a large variety of applications. However, obtaining well-dispersed metal nanoparticles on the surface of the solid support is a challenge, although different methods are described in the literature, such as impregnation, adsorption, ion exchange, sol–gel, and co-precipitation. Generally, the drawback of these methods is either agglomeration of the metal nanoparticles or poor metal–support interaction. The application of nitrogen-doped carbon materials as supports should avoid these problems because the pyridine nitrogen atoms not only may provide the main initial nucleation sites for the formation of small and highly dispersed metal nanoparticles, but also may reduce the leaching of the metal nanoparticles during catalysis, due to strong nitrogen–metal bonding. For the energy conversion, development of non-noble-metal-based catalysts with fine dispersion of small nanoparticles on a nitrogen-rich ordered mesoporous carbon support is desirable from both economics and engineering points of view. Although catalysts based on noble metals, such as Pt and Pd, been widely studied as hydrogenation catalysts, in spite of good catalytic performance under mild conditions, their application is restricted because of their limited availability and high costs [28]. Actually, in industrial applications, Ni rather than noble metals is usually chosen as a catalyst for the hydrogenation reaction, owing to its abundant availability and the economics involved. Therefore, nitrogen-rich carbon material with fine dispersion of small nickel nanoparticles has efficient catalytic ability for hydrogenolysis of HMF to DMF with high selectivity. Increasing environmental concern arises because of the adverse effects associated with use of organic solvent, creating demand for greener solvents such as water. The effective use of water as a solvent in selective hydrogenation reactions is not only environmentally beneficial but also economically viable [29]. To carry out reactions practically in aqueous media, the catalyst should have sufficient mechanical stability or metal–support interactions to resist leaching of active metals. It has already been proven that doping of nitrogen atoms in Pd-supported mesoporous carbon material provides a hydrophilic nat-

ure to the material, which is very helpful in enhancing catalytic performance for upgrading of bio-oil [28].

In this report, we are presenting a facile synthesis methodology for a nanodispersive hydrophilic Ni catalyst and for an environmentally as well as economically sustainable process for selective hydrogenation of 5-HMF to DMF (Scheme 1). Moreover, we have tried to correlate the catalytic activity, selectivity, and stability with particle size distribution and strong interfacial interactions among metal nanoparticles, nitrogen functionalities of the support material, and hydrophilicity of the material. DFT analysis has been carried out to evaluate possible reaction mechanisms for this newly developed catalytic material.

## 2. Experimental

### 2.1. Materials

Tetraethylorthosilicate (TEOS), poly(ethylene oxide)-block-poly(propylene oxide)-block-poly(ethylene oxide) triblock copolymer (Aldrich, MW avg. 5800, EO20PO70EO20, P123), ethylenediamine ( $\text{NH}_2\text{C}_2\text{H}_4\text{NH}_2$ ), nickel nitrate ( $\text{NiNO}_3 \cdot 2\text{H}_2\text{O}$ ), tetraammineplatinum(II) nitrate [ $\text{Pt}(\text{NH}_3)_4(\text{NO}_3)_2$ ], and palladium(II) chloride ( $\text{PdCl}_2$ ) were purchased from Sigma–Aldrich Co. Ethanol, carbon tetrachloride ( $\text{CCl}_4$ ), NaOH, HCl, and urea were purchased from Merck KGaA, Darmstadt, Germany. All the chemicals were used without further purification. Double-distilled water was prepared with a BOROSIL water distillation unit.

### 2.2. Material synthesis

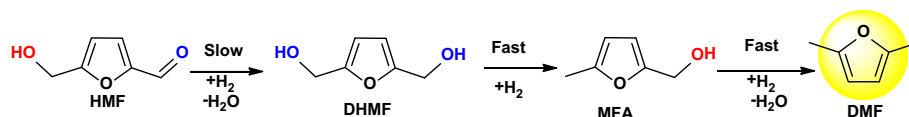
Ni-supported mesoporous nitrogen-rich carbon material was synthesized using SBA-15 as a hard template. SBA-15 was prepared using a literature-reported method without further modification.

#### 2.2.1. Synthesis of SBA-15

To synthesize SBA-15, TEOS is used as silica source and P123 as surfactant. First 4.0 g of P123 was dissolved in 40 ml of deionized water under continuous stirring. After that, 120 ml of 2 M HCl was added to make the solution acidic with 4 h of stirring. A portion of 9.1 g of TEOS was added dropwise under agitation. The solution was kept for 24 h under the same conditions. The obtained mixture was transferred to a Teflon-lined autoclave for hydrothermal treatment at 100 °C for 48 h. After cooling to room temperature the solid products were filtered, washed with water, and dried in a 60 °C oven. Finally, the material was calcined at 550 °C (ramp rate 3 °C/min) for 6 h in air flow.

#### 2.2.2. Synthesis of $\text{MCN}_x$

To synthesize Ni-supported mesoporous nitrogen-rich carbon material, 1 g of calcined SBA-15 was taken in a round-bottomed flask with 11 g of  $\text{CCl}_4$  solvent and 4.4 g of ethylenediamine. To polymerize this mixture, it was refluxed at 90 °C for 6 h. To carbonize the product, it was treated at 600 °C under nitrogen for 6 h. To remove the silica from the obtained product, the silica/carbon/nitrogen mixture was treated with a 2.5 wt.% NaOH 1:1 ethanol–water mixture at 100 °C for 3 h, and then filtered and washed with 3–4 L water until it reached pH 7. The process was repeated 2–3 times.



Scheme 1. Schematic hydrogenation pathway for HMF to DMF.

### 2.2.3. Preparation of mesoporous carbon

Mesoporous carbon (MC) has been prepared by the process reported in the literature [30]. A portion of 1 g of SBA-15 was added to a solution of 1 g sucrose and 0.12 g H<sub>2</sub>SO<sub>4</sub> in 5 ml of H<sub>2</sub>O. The obtained mixture was placed in a 110 °C oven for 6 h and subsequently the temperature was raised to 160 °C and maintained for another 6 h. The heat treatment was repeated again after addition of 0.6 g sucrose and 0.09 g H<sub>2</sub>SO<sub>4</sub> in 5 ml H<sub>2</sub>O. The obtained sample was carbonized under N<sub>2</sub> at 900 °C for 5 h. The silica template was removed per the process mentioned above.

### 2.2.4. Preparation of Ni-OMD and Ni-OMDC catalysts

We have followed two main routes (organic matrix deposition and chelation) to synthesize Ni nanoparticles on a CN<sub>x</sub> network. To deposit the nickel nanoparticles on two different supports, 1 g of MCN<sub>x</sub> or MC was taken in 1 L of water. Nickel nitrate was added in different ratios (1:2:3) to completely solubilize the solution it was stirred. After 1 h, nickel urea was added to it three times for slow reduction. The solution was kept at 60 °C for 48 h under vigorous agitation. Finally, the obtained product was filtered, washed, and dried.

### 2.2.5. Preparation of Ni-CA catalysts

To synthesize the Ni-CA catalyst, Ni acetyl acetonate in different ratios (3 and 5 wt.% to bare CN<sub>x</sub>) dissolved in a minimum amount of water and citric acid was added 20 times (mole) of Ni. After continuing stirring for 6 h at 60 °C, the solvent was evaporated, and subsequently ethanol was added to the above mixture. The pH of the solution was maintained (pH up to 8) using ammonia. A portion of 1 g of CN<sub>x</sub> was added under stirring and finally the solvent was evaporated and dried overnight. Calcination was performed under N<sub>2</sub> at 400 °C for 3 h to obtain the Ni-CA catalyst.

### 2.2.6. Preparation of Pt-OMD1 and Pd-OMD1 catalysts

To deposit platinum nanoparticles on mesoporous nitrogen-rich carbon material, 1 g of MCN<sub>x</sub> was taken in 1 L of water. Palladium and platinum nitrate 1% were added to it to completely solubilize the solution as it was stirred. After 1 h, 3 times the metal urea was added to it for slow reduction. The solution was kept at 60 °C for 48 h under vigorous agitation. Finally, the obtained product was filtered, washed, and dried.

## 2.3. Catalyst characterization

The prepared mesoporous nitrogen-rich carbon materials were characterized by N<sub>2</sub> physisorption measurements at 77 K using an Autosorb 1C setup (Quantachrome) adsorption analyzer. Prior to the measurements, the samples were degassed under vacuum ( $1 \times 10^{-5}$  Torr) for 2 h at 200 °C. The BET specific surface areas were determined from the adsorption data in the relative pressure ( $P/P_0$ ) range of 0.06–0.2. The pore size distributions (PSDs) were calculated from the nitrogen adsorption branch using the Barrett–Joyner–Halenda (BJH) method and the maximum of the PSD was considered as the average pore size. The pore volume was considered as the volume of liquid nitrogen adsorbed at  $P/P_0 = ca. 1$ . The morphology of the Ni/MNC<sub>x</sub> materials synthesized at different temperatures and different loadings of nickel was investigated using SEM and HRTEM. Scanning electron microscopy (SEM) images were taken on an FEI Quanta 200 F instrument, using tungsten filaments doped with lanthanum hexaboride (LaB<sub>6</sub>) as an X-ray source, fitted with an ETD detector with a high vacuum mode using secondary electrons and an acceleration tension of 10 or 30 kV. Images were recorded at various magnifications. All the samples were analyzed by spreading them on a carbon tape and coated with gold to increase the electrical conductivity. A JEOL JEM 2100 high-resolution transmission electron microscope

(HRTEM) was employed to see the porous nature of the material. Energy-dispersive X-ray spectroscopy (EDX) was used in connection with TEM for the elemental analysis. The elemental mapping was also collected with the same spectrophotometer. Samples are mounted by dispersing them on ethanol on a lacey carbon Formvar-coated Cu grid. Low and wide-angle powder X-ray diffractograms (XRD) were obtained with a D8-Advance-Bruker-AXS diffractometer (Cu K $\alpha$  radiation;  $\lambda = 1.5418 \text{ \AA}$ ) in  $\theta$ – $2\theta$  geometry and with a position-sensitive detector (capillary technique, thickness 1 mm).

X-ray photoelectron spectroscopy (XPS) measurements were carried out in an ultra-high-vacuum (UHV) setup equipped with a monochromatic Al K $\alpha$  X-ray source ( $h\nu = 1486.6 \text{ eV}$ ), operated at 14.5 kV and 35 mA, and a high-resolution Gamma data-Scienta SES 2002 analyzer. The base pressure in the measurement chamber was maintained at about  $7 \times 10^{-10}$  mbar. The measurements were carried out in the fixed transmission mode with pass energy 200 eV, resulting in an overall energy resolution of 0.25 eV. A flood gun was applied to compensate for the charging effects. Resolution spectra for C1s, O1s, and N1s were recorded. The binding energy scales were recalibrated based on the  $sp^2$  hybridized C1s line of graphitic carbon at 284.5 eV. Casa XPS software with a 70:30 Gaussian–Lorentzian product function and Shirley background subtraction was used for peak deconvolution. The obtained spectra from different elements were plotted using the same intensity scale for all the analyzed samples to facilitate comparison. Temperature-programmed reduction (TPR) of the catalyst was carried out using 10% H<sub>2</sub> in a He flow as the reducing agent in a Micromeritics Auto Chem II 2920 instrument. The amount of H<sub>2</sub> consumed during the reduction was estimated on the basis of the analysis with a thermal conductivity detector. The gas flow rate was 30 mL/min. The weight of the sample was 25 mg, and the heating rate of TPR was 20 °C/min. To understand the reaction mechanism and the stability and selectivity of the catalyst, we have performed a density functional (DFT) [31] study using the Gaussian 09 [32] package. Geometries of the reactant, products, and intermediates are optimized without any symmetry constraints and checked by harmonic vibrational frequency analysis (i.e., with all positive frequencies). Transition states for two different pathways are confirmed by one imaginary mode of vibration along suspected bond breaking and bond making. Activation energies for these two transition states are calculated from free energy differences between the transition states and the reactants. The convergence thresholds for convergence are set to 0.000015 Hartree/Bohr for the forces, 0.00006 Å for the displacement, and 106 Hartree for the energy change. Unrestricted Becke's three parameters hybrid with exchange functional [33] combined with the exchange component of the Perdew and Wang's 1991 functional [34–37]. Abbreviated as B3PW91, it is used for DFT calculations. Lan12dz [38] basis sets are used for all calculations that are available in the Gaussian 09 package. We used this basis because for nickel (Ni), only this series of basis functions are available.

## 2.4. Hydrogenation of HMF

Hydrogenolysis of HMF was carried out in a 100 ml stainless steel batch reactor (Parr made) fitted with a mechanical stirrer. In a typical experiment 10 ml HMF (2 mmol) solution with 50 mg of catalysts was added to 10 ml of water in a stainless steel reactor. Prior to the reaction, each catalyst was reduced with 10% H<sub>2</sub>, balance He, for 1 h and transferred to the reactor. The reactor was purged twice with hydrogen and finally 3.0 MPa of H<sub>2</sub> was maintained after the outlet valve was closed. The reaction was performed in the temperature range 60–200 °C for 1–6 h under continuous stirring at 400 rpm. The reaction aliquots were collected at different intervals. After the completion of the reaction,

the reaction was allowed to cool down at room temperature. The reaction mixture was filtered and decanted into a separating funnel. Different products were separated using column chromatography, the ethanol/ethyl acetate mixture was used as the mobile phase and the recovered sample was dried with a drying agent such as activated sodium sulfate. All the products were analyzed through GC-MS (HP) fitted with an HP-5 capillary column. The activity of the catalyst was calculated as

$$\text{Conversion (C\%)} = \frac{\text{Moles of reactant reacted (C\%)}}{\text{Moles of reactant initially used (C\%)}} \times 100,$$

$$\text{Selectivity (C\%)} = \frac{\text{Moles of product (C\%)}}{\text{Moles of reactant reacted (C\%)}} \times 100.$$

### 3. Results and discussion

#### 3.1. Structural characterization of Ni-supported catalysts

The structural evaluation of material has been performed using an X-ray diffractometer. The low-angle XRD pattern of the material (Ni-OMD) as well as of the support  $\text{CN}_x$  shows (in Fig. 1a) peaks at  $0.96^\circ$  and two small intense peaks in the region  $2\text{--}3^\circ$ , which were indexed to the (100), (110), and (200) reflections of the hexagonal  $p6mm$  space group. The presence of these three peaks in small-angle regions evidenced the mesoporous nature of the material. The (100), (110), and (200) planes reveal the ordered hexagonal porous nature of the material, which can also be seen from TEM images and the  $\text{N}_2$  adsorption isotherm (discussed later). Ni-OMD3 and Ni-OMD5 shows shifting of peaks toward higher  $\theta$  values with the loss of peak intensity, which means an increasing  $d$

value indicating a decrease in the pore size of the material. Ni-CA3, in Fig. S1 (in the Supporting Information), shows only two peaks at  $\theta$   $0.98^\circ$  (100 plane) and  $1.42^\circ$  (110 plane); a huge loss in peak intensity corresponding to the (100) plane can be visualized as compared with Ni-OMD3. It can be concluded that the ordered nature of the material is somewhat lost when citric acid is used for deposition of Ni nanoparticles. In the wide-angle XRD pattern of the Ni-OMD3, no peaks for any kind of Ni species have been observed, which indirectly indicates the presence of finely dispersed Ni nanoparticles on the  $\text{CN}_x$ . When the catalyst was reduced for 1 h in a 10%  $\text{H}_2$  environment, the catalyst shows (in Fig. 1b) two broad peaks concentrated at  $44.45^\circ$  and  $51.73^\circ$  for Ni (111) and Ni(200), respectively [39]. The small-angle diffraction pattern for the used catalyst (Fig. S2 in the Supporting Information) shows that the mesoporous nature of the material is unaffected during the reaction. The peaks at  $2\theta = 37.6^\circ$  and  $43.7^\circ$  can be indexed as NiO (JCPDS card No. 47-1049) and the diffraction peaks at  $2\theta = 44.8^\circ$  and  $52.2^\circ$  can be indexed to Ni (JCPDS card No. 87-0172), which suggests that NiO has formed along with Ni $^\circ$  on the Ni-OMD catalyst during reaction. However, the material prepared using a chelation method (Ni-CA) shows peaks for Ni–O crystalline planes due to the large particle size of Ni–O nanoparticles, which can also be seen from TEM images.

$\text{N}_2$  adsorption–desorption of the material shows (in Fig. 1c) mostly an H1 type hysteresis loop and a type IV isotherm, which is a characteristic isotherm for mesoporous material. The steepness in the hysteresis loop reveals the ordering in the porous nature of the material, while the shifting of the isotherm at a somewhat higher value from  $P/P_0$  0.39 (for Ni-OMD5) to 0.44 (for mesoporous  $\text{CN}_x$ ) further confirms the presence of larger pores in Ni-OMD catalyst than for  $\text{CN}_x$ . The surface area of the mesoporous  $\text{CN}_x$  is  $586.0 \text{ m}^2/\text{g}$  (see Table 1). With increasing Ni loading the BET

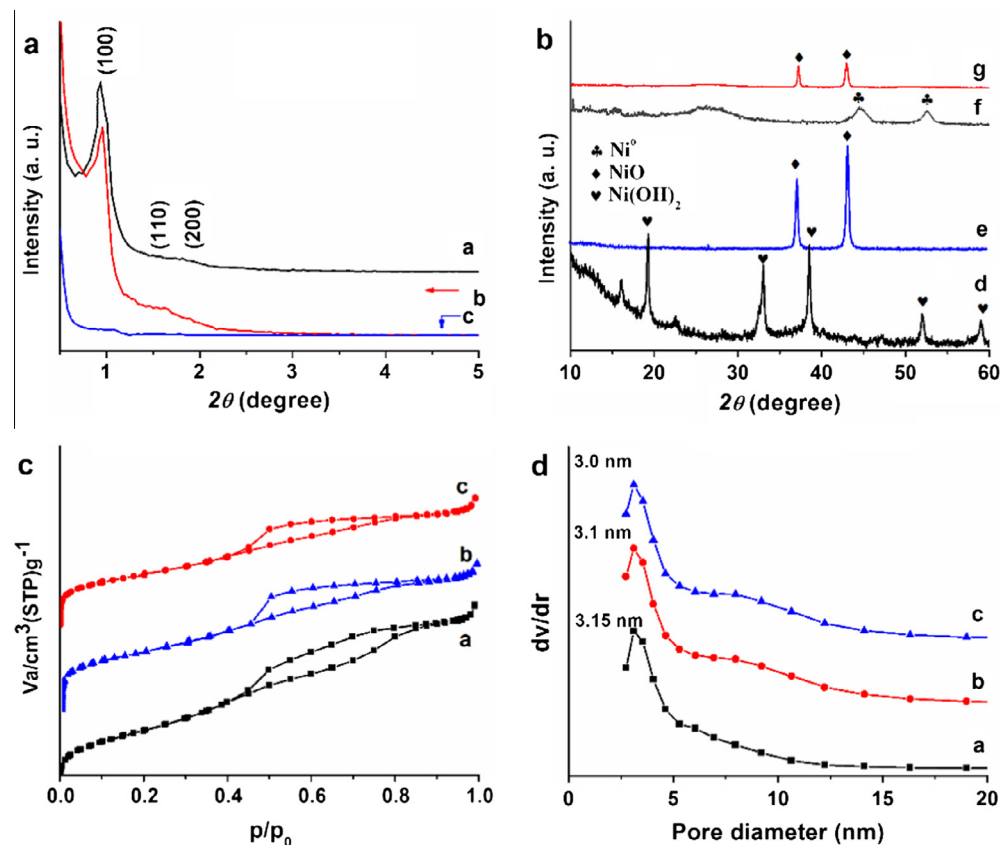


**Fig. 1.** (a) Low-angle and (b) wide-angle XRD pattern of the studied material; (c) and (d) BET adsorption–desorption isotherm and pore diameter, respectively. a = ordered mesoporous  $\text{CN}_x$ ; b = Ni-OMD3; c = Ni-OMD5; d = pure  $\text{Ni}(\text{OH})_2$ ; e = pure NiO; f = reduced Ni-OMD3; and g = Ni-CA3.

surface area drops to 535.5 m<sup>2</sup>/g for Ni-OMD3 and 448.1 m<sup>2</sup>/g for Ni-OMD5, respectively. It has also been observed that a small decrease in total pore volume with increasing in nickel concentration might be due to blockage of available pores by nickel nanoparticles with increased Ni loading. The BJH (Barrett–Joyner–Halenda) shows a pore diameter (Fig. 1d) of 3.15 nm for ordered mesoporous CN<sub>x</sub> material, whereas high metal loading results in a decrease in pore diameter, showing pore filling by Ni nanoparticles. However, the Ni-CA3 (Fig. S3 in the Supporting Information) also shows H1 type hysteresis and a type IV isotherm; however, the order in hysteresis loop is found not to be very nice and the surface area and total pore volume (in Table 1) of the material also appeared to be low compared with Ni-OMD.

To further understand the porous nature and structure of the material, we have taken the HR-TEM and SEM images of material and shown them in Figs. 2 and 3a and b, respectively. The TEM images (Ni-OMD1, 3, and 5) show the wheatlike morphology of the material, with regular arrays of strips. TEM images also clearly indicate the highly porous nature of the material. The presence of nickel oxide nanoparticles cannot be observed for Ni-OMD1, but for Ni-OMD3 and Ni-OMD5 very small and highly dispersed nickel nanoparticles are observed, from which it can be assumed that nickel oxide particles are present inside the pores. The HR-TEM images of the spent catalyst show the presence of highly dispersed Ni<sup>0</sup> in the catalyst system; the co-presence of NiO appears as scattered black shadows over the catalyst (Fig. S4 in the Supporting Information). The elemental mapping along with the EDX spectra shows very homogeneous dispersion of Ni over the catalyst surface. The EDX microanalysis report (Fig. S5) additionally shows the presence of 2.48 wt.% Ni on the Ni-OMD3 catalyst, which proves that there is no or negligible leaching of Ni particles during the reaction (as compared with the data of Table 1 for the fresh catalyst). The TEM images of nickel nanoparticles supported on mesoporous carbon (Ni-OMDC) materials have very large nickel particles, between 15 and 40 nm (Fig. S6). The HRTEM elemental mapping of the Ni-OMD3 shows (Fig. 4) a very homogeneous distribution of Ni within the CN<sub>x</sub> framework. With the increase in metal loading in the sample, some amount of nickel oxide may remain on the surface as well as the particle size increasing (as evidenced from HR-TEM in Fig. S7). The TEM images of the material prepared using a chelation (Ni-CA3) method have irregular morphology; the wheatlike structure of the material is getting distorted, as well as ordering in pores also getting disturbed, Fig. 2. Nickel nanoparticles appear to be agglomerated with large average particle size (Fig. S8 in the Supporting Information).

### 3.2. Nature of nickel species supported on CN<sub>x</sub> and their reducibility

An XPS experiment was performed to determine the surface composition of the Ni-OMD3 catalyst. The XPS survey spectrum confirms the presence of mainly Ni, C, N, and O in the catalyst (Fig. S9 in the Supporting Information). The Ni2p XP spectra of

the prepared catalyst show two main peaks, one at 856.1 and another at 873.5 eV, corresponding to the presence of Ni(OH)<sub>2</sub> within the catalyst [40–42]. When the Ni-OMD3 catalyst was reduced prior to the experiment, nickel was found in the metallic state (Fig. 4c and d). However, as we can see from the Ni2p XP spectra of the spent catalyst, Ni resides as NiO in the spent catalyst (Fig. S10 in the Supporting Information). A positive shift of 0.4 eV in the Ni2p binding energy is also experienced, which may be due to enhanced interfacial interaction between Ni and the nitrogen atoms of the CN<sub>x</sub> framework. This observation evidenced that Ni<sup>0</sup> is the active species for the reaction, and after the reaction, these metallic Ni species interact with H<sub>2</sub>O (present as reaction medium) to form NiO species. Moreover, the Ni-OMC catalyst also had a binding energy of 855.26 eV (Fig. S11 in the Supporting Information), which clearly indicate the absence of any interaction between nickel particles because of the absence of nitrogen. The Ni-CA catalyst has Ni2p binding energy slightly higher than Ni-OMC, which may be due to very small interaction. The ICP analysis data show a small amount of Ni in the Ni-OMC3 catalyst. The observations further confirm the low metal–support interfacial interaction, which directly helps to stabilize the Ni catalyst synthesized through the OMD method.

The C1s spectrum of as-synthesized catalyst can be deconvoluted into five peaks (Fig. 5a). The two intense peaks at 284.5 and 285.4 eV binding energy may be assigned to sp<sup>3</sup> hybridized graphite-like carbon and sp<sup>2</sup> hybridized diamond-like carbon, respectively [25,43], whereas two other peaks at 286.5 and 288.5 eV show the presence of surface oxygen functionalities such as CO, C=O. The peak at 289.8 eV may be assigned to C–N type structural units present in the catalyst. The N1s spectra of the Ni-OMD3 catalyst exhibit four main peaks (Fig. 5b). The small peak at the lowest binding energy, 397.5 eV, may be assigned to Ni–N interaction [42]. The peaks at 398.9, 400.1, and 403.5 eV are related to the presence of N-pyridine, N-pyrolic, and N-quaternary structure in the catalyst. However, in the catalysts prepared by the chelation method (Ni-CA3 and Ni-CA5), the Ni2p binding energy found at 855.7 and 855.9 eV indicates the presence of Ni(OH)<sub>2</sub> within the catalyst (Fig. S12 in the Supporting Information) [44]. A small negative shift in the binding energy of Ni<sup>2+</sup> in Ni(OH)<sub>2</sub> may be due to the loss of Ni–N interaction in the Ni-CA catalyst. This is also evidence that, during the hydrogenation reaction, the catalysts prepared via the chelation method (Ni-CA3 and Ni-CA5) show leaching of Ni species. This observation can be explained by the significant interfacial interaction between Ni and nitrogen within the catalyst; on lowering of interaction the Ni species comes out of the CN<sub>x</sub> framework, which causes leaching and Ni–Ni agglomeration. In order to verify the conclusion, we have taken TEM images of the catalyst (Ni-CA3 and Ni-CA5) after reaction and found heavy agglomeration of Ni species over the support CN<sub>x</sub>. We performed Sheldon's [45] hot filtration test, which involves filtration of the catalyst partway through the reaction,

**Table 1**  
Physicochemical properties of the catalyst.

Materials	Surface area [m <sup>2</sup> /g] <sup>a</sup>	Metal dispersion (%) <sup>b</sup>	Ni conc. [wt.%] <sup>c</sup>	N conc. [wt.%] <sup>d</sup>	Pore volume [a]
CN <sub>x</sub>	586.0	–	–	13.41	0.682
Ni-C3	511.3	12.1	–	–	0.542
Ni-OMD3	535.5	46.2	2.47	12.53	0.555
Ni-OMD5	448.1	25.9	4.83	13.01	0.305
Ni-CA3	491.3	17.6	2.21	12.82	0.348

<sup>a</sup> Determined by nitrogen physisorption and calculated by the BET method.

<sup>b</sup> Calculated from H<sub>2</sub> chemisorption analysis.

<sup>c</sup> Calculated from ICP-AES.

<sup>d</sup> N content was calculated from CHNS analysis.

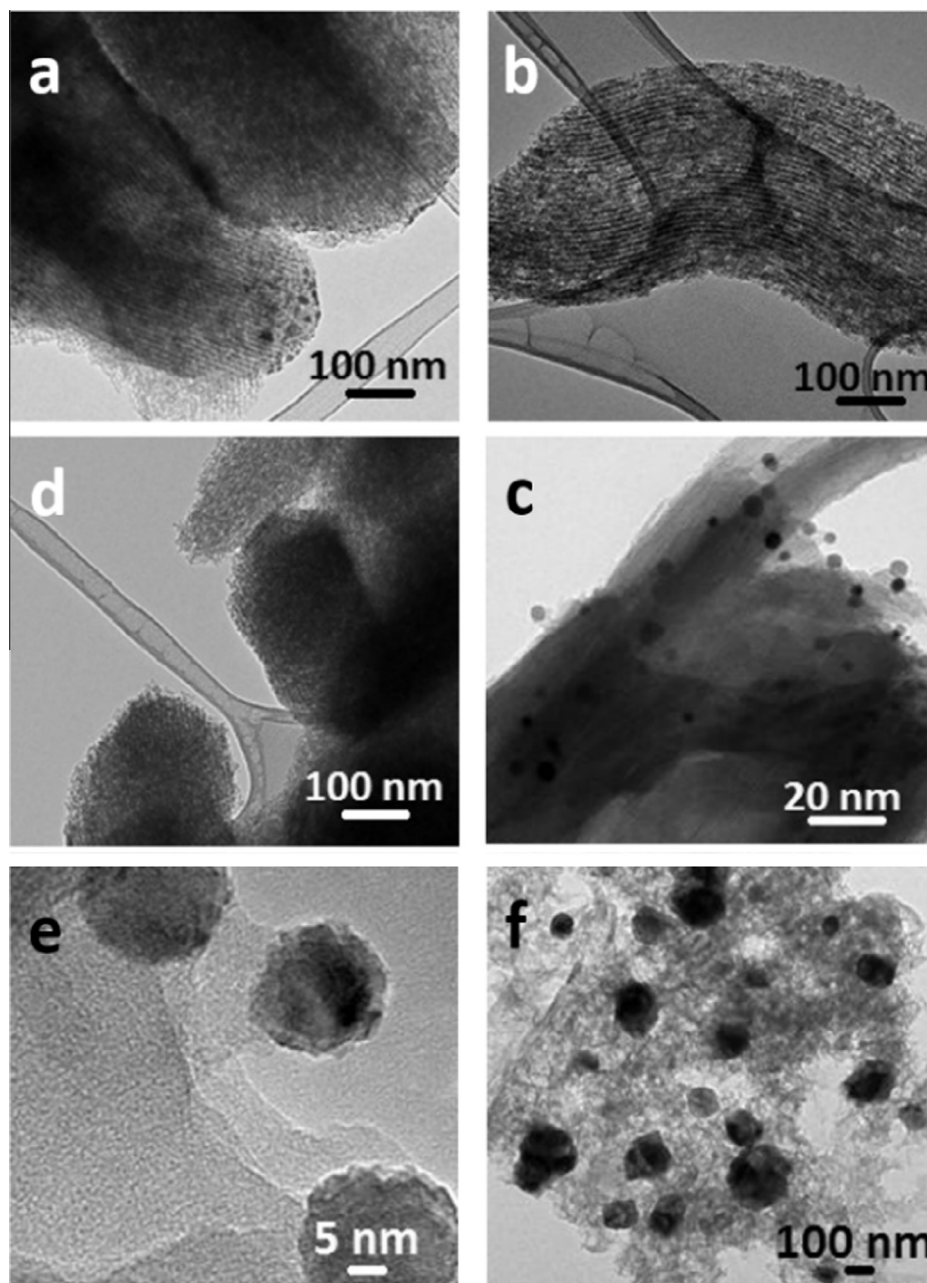


Fig. 2. HR-TEM images of (a) Ni-OMD1; (b, c) Ni-OMD3; (d) Ni-OMD5; (e) Ni-CA3; and (f) Ni-CA5.

followed by continuation of the reaction in the absence of the catalyst. The result shows no further reaction in the absence of the catalyst after filtration. Additionally, the hot filtrate was subjected to ICP analysis. The test shows a negligible presence of Ni, at the ppb level, which also proves the heterogeneity of the present catalyst system.

Comparative Raman spectra of Ni-CA3 and Ni-OMD3, as well as reduced Ni-OMD3, have been provided in Fig. 5C. In general, all carbons show common features of their Raman spectra in the region  $800\text{--}2000\text{ cm}^{-1}$ , and the so-called G and D bands lie at around  $1596$  and  $1320\text{ cm}^{-1}$ , respectively, for visible excitation [46]. In the present study, we experienced a significant shift of G and D bands for the catalyst prepared by an organic template and citric acid deposition method. The shift of  $38\text{ cm}^{-1}$  for graphitic peaks of Ni-CA3 and Ni-OMD3 indicates the nitrogen-rich environment of the  $\text{CN}_x$  network [47], whereas only a  $6\text{ cm}^{-1}$  shift was

observed for the position of the D-band in Ni-CA3 and Ni-OMD3 catalysts, which may be due to charge transfer between  $\text{Ni}(\text{OH})_2$  and  $\text{CN}_x$ . For the reduced catalyst this D-band again showed a shift of  $5\text{ cm}^{-1}$ ; this could be due to the charge transfer between metallic Ni and  $\text{CN}_x$ , which is entirely different from the charge transfer between  $\text{Ni}(\text{OH})_2$  and  $\text{CN}_x$ .

Fig. 5D shows the  $\text{H}_2$  TPR profiles of different Ni-OMD catalysts along with a commercial nickel(II) nitrate sample. For synthesized Ni-OMD3 catalyst, a broad peak at  $292\text{ }^\circ\text{C}$ , the temperature at maximum reduction ( $T_m$ ), with a shoulder peak centered at  $466\text{ }^\circ\text{C}$  is observed. For higher loading of Ni in mesoporous  $\text{CN}_x$ , e.g., Ni-OMD5, the peak shifted toward higher value and appeared at  $T_m$   $431\text{ }^\circ\text{C}$  along with a shoulder peak, which is very difficult to isolate. Nevertheless, the peak spanning after  $650\text{ }^\circ\text{C}$  is due to the parent  $\text{CN}_x$  framework (Fig. S13 in the Supporting Information). In comparison, in the Ni-OMD catalyst, Ni in nickel(II) nitrate is reduced

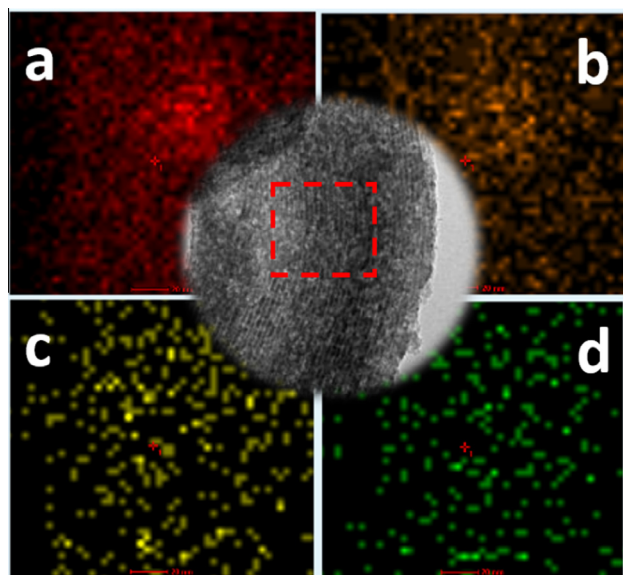


**Fig. 3.** HRTEM elemental mapping of (a) carbon, (b) nitrogen, (c) oxygen, and (d) nickel. Inset: the corresponding TEM of the Ni-OMD catalyst.

at a higher temperature,  $T_m$  of 636 °C, along with a shoulder peak at  $T_m$  703 °C. Therefore, the two hydrogen consumption peaks of Ni-OMD3 at lower temperature can be correlated with the smaller size of Ni particles dispersed in the porous network of  $CN_x$  compared with Ni-OMD5 and nickel(II) nitrate; hence they are easy to reduce. In general,  $T_m$  is dependent on the particles' size, i.e., smaller particles are expected to be reduced at lower temperature. The two hydrogen consumption peaks in the directly synthesized sample can be ascribed to the reduction of fine Ni nanoparticles highly dispersed at the porous surface of the mesoporous composite (at 292 °C) and bulk Ni species (at 466 °C), respectively. In case of the Ni-OMDC catalyst, we have observed a reduction peak at

440 °C with a small shoulder following. The shift in reduction peaks to higher temperature is due to absence of interaction between large nickel particles and support (Fig. S14). Similarly, when we look at the Ni-CA catalyst, we observed a positive shift of >120 °C from Ni-OMD catalyst (Fig. S15 in the Supporting Information). For Ni-CA3, a broad peak at a temperature at maximum reduction  $T_m$  of about 416 °C with a shoulder peak above 650 °C is observed. Upon higher loading by the chelation method (i.e., Ni-CA5), the  $T_m$  shifts further to high value at 431 °C. With all these observations, due to the absence of interaction (which arises between nitrogen and metallic nickel because of the very small particles formed by the OMD method) in Ni-OMDC and Ni-CA catalysts, the reduction temperature is shifted to higher values. Moreover, it can be considered that the organic matrix deposition method is more appropriate to design highly dispersed Ni nanoparticles over mesoporous  $CN_x$  (not on mesoporous carbon) than the chelation method.

### 3.3. Effect of preparation method on nickel concentration

Nickel concentrations in catalysts prepared by organic matrix deposition and citric acid deposition were measured by ICP and are shown in Table 1. Nickel concentration was found to be higher in catalysts prepared by organic matrix deposition method than in those prepared by reduction by citric acid. Comparison indicates that the difference in nickel loading can be ascribed to the different interaction between nickel species and the support  $CN_x$  [48].

According to the electrostatic adsorption model, the pH of the solution, the zero point charge (PZC) of the support, and change of the adsorbing ion have a marked influence on metal deposition [49]. The support PZC can be taken as equivalent to its slurry; the adsorption of cations is favored if the pH of the system is higher than that of the PZC of the support [50]. Hence for the organic matrix deposition method, the pH of the deposition medium was higher than the PZC of the support  $CN_x$  (in Table S1, Supporting Information). As negatively charged supports favor attracting and adsorbing

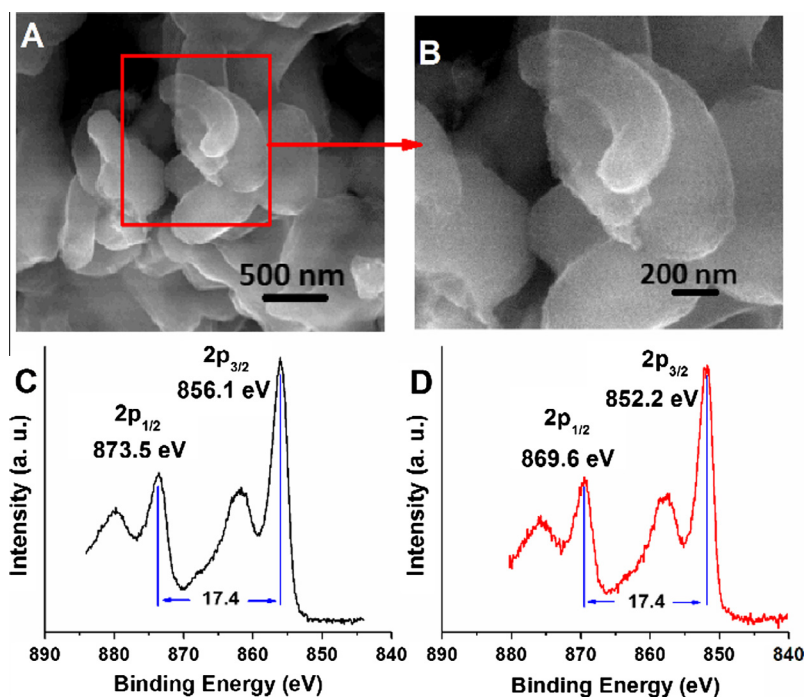


**Fig. 4.** (a, b) SEM images of Ni-OMD3 at different magnifications; (c) Ni<sub>2p</sub> XP spectra of the prepared Ni-OMD3 and (d) Ni<sub>2p</sub> XP spectra of the Ni-OMD3 catalyst after reduction, prior to the reaction.

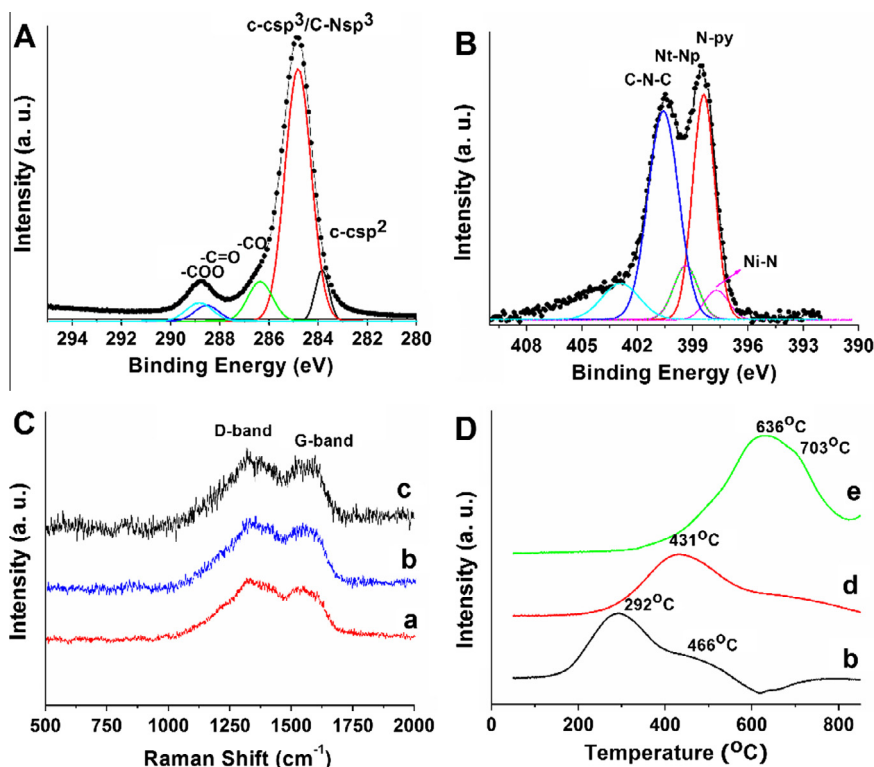


**Fig. 5.** (A) C1s and (B) N1s XP spectra of the Ni-OMD3 catalyst; (C) Raman spectra and (D) TPR pattern of different Ni-CN<sub>x</sub> catalysts. a = Ni-CA3, b = Ni-OMD3, c = Ni-OMD3 after reaction, d = Ni-OMD5, and e = Ni(NO<sub>3</sub>)<sub>2</sub>.

positively charged Ni cations, nickel concentration in the Ni-OMD catalyst was higher, whereas the acidic nature of citric acid neutralized the negative charges of the support material (in Table S1), which causes a decrease in electrostatic attraction and hence a lower nickel loading on CN<sub>x</sub>. Additionally, the difference in reducing strength of citric acid compared with that of organic matrix also accounted for the difference in Ni content in the catalyst.

### 3.4. Hydrogenation activity

The results of the hydrogenation of HMF with elevated H<sub>2</sub> pressure to DMF in aqueous media are presented in Table 2. The support material, mesoporous CN<sub>x</sub>, shows only 9.8% HMF conversion (entry 2) with negligible DMF selectivity, whereas the reaction without any catalyst shows 3–4% HMF conversion. In this study we mainly concentrate on deposition of Ni with various reducing agents. The catalyst prepared by organic matrix deposition shows higher activity than for other methods (discussed earlier). The Ni-OMD3 catalyst shown 89.7% HMF conversion with 99.1% DMF

selectivity after 4 h of reaction; when the reaction is prolonged further to 6 h, the conversion reaches over 99.9% with 98.7% DMF selectivity. The Ni-CA3 catalyst shows only 70.3% HMF conversion with 69.9% DMF selectivity. This could be due to bigger crystallite size of Ni partials in the Ni-CA3 catalyst, which is hard to reduce (as shown in Fig. 6) or lower in Ni concentration (Table 1) in the catalyst compared with Ni-OMD3.

Over the past decade, noble metals such as Pt and Pd supported on activated carbon have been recognized as the best hydrogenation catalysts. Therefore, we have compared our results (Ni catalyst) with noble-metal-based catalysts prepared via organic matrix deposition and found Pt is more active (entry 6) than Pd when deposited on CN<sub>x</sub>. The latter shows relatively better DMF selectivity than the former, but the Ni-OMD catalyst shows higher DMF conversion and selectivity than both. Nickel nanoparticles supported on CNT prepared using the reported method (Table 2, entry 11) are found to be much less active and selective. The catalytic activity of the Ni-OMD catalyst was also compared with that of the reported catalyst system (entries 8–10) [6,51–53]. Among

**Table 2**  
Catalytic activity of different catalysts on HMF hydrogenation to DMF.

Entry	Catalyst	<i>t</i> [h]	Solvent	Conversion	DMF selectivity	<i>E</i> <sub>o</sub> <sup>a</sup>	TOF (h <sup>-1</sup> )	Ref.
1	Blank	6	H <sub>2</sub> O	3–4	<1	0.04	–	This work
2	CN <sub>x</sub>	4	H <sub>2</sub> O	9.8	<1	0.09	–	This work
3	Ni-OMD3	4	H <sub>2</sub> O	89.7	99.1	9.32	438.7	This work
4	Ni-OMD3	6	H <sub>2</sub> O	>99.9	98.7	9.32	325.7	This work
5	Ni-CA3	6	H <sub>2</sub> O	70.3	69.9	6.52	229.2	This work
6	Pt-OMD1	6	H <sub>2</sub> O	99.0	62.9	5.87	3218	This work
7	Pd-OMD1	6	H <sub>2</sub> O	86.7	89.6	8.36	1537	This work
8	Pd/C/Zn	8	THF	>99.0	85.0	1.19	27.2	[6]
9	Rh/C	6	IPA	>99.0	81.0	NA	8.55	[50]
10	Pd/C	15	THF	–	70.0	NA	NA	[51]
11	Ni/CNT	6	H <sub>2</sub> O	45.0	32.5	NA	26.2	[52]

Notes: 20 ml of 0.1 M HMF solution in H<sub>2</sub>O, 0.05 g reduced catalyst, temperature 200 °C, H<sub>2</sub> 30 bar.

<sup>a</sup> *E*<sub>o</sub>: H<sub>2</sub> efficiency calculated by (100 × moles of DMF formed)/total moles of H<sub>2</sub> added. Moles of H<sub>2</sub> added was calculated using the ideal gas equation.

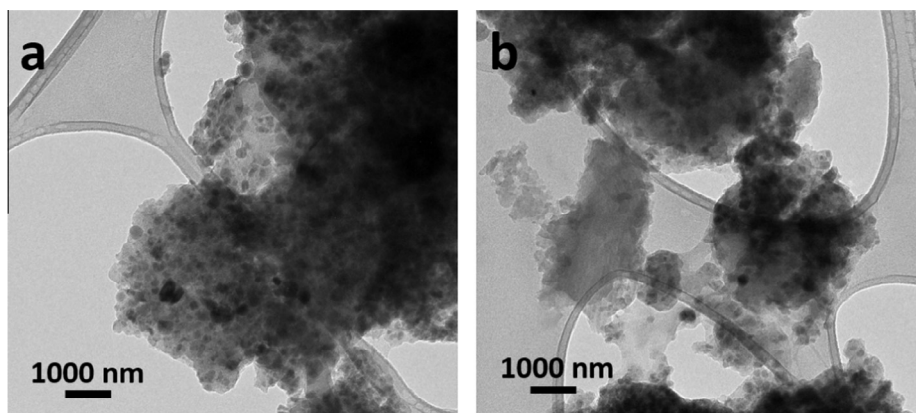


Fig. 6. HRTEM images of (a) Ni-CA3 and (b) Ni-CA5 catalyst after the hydrogenation reaction.

the reported catalyst systems Pd/C (entry 10) uses a secondary source of H<sub>2</sub> (generates H<sub>2</sub> from formic acid) and achieved 70% HMF conversion. We report a non-noble-metal catalyst for hydrogenation of HMF with ~99% conversion with 98.7% DMF selectivity in equal or less time on stream. Moreover, the H<sub>2</sub> efficiency ( $E_o$ ) has been calculated and a very high  $E_o$  value (9.32) has been found for the Ni-OMD catalyst, although Pd-OMD1 shows a good H<sub>2</sub> efficiency of 8.36 still limited by its selectivity toward DMF. This comparison suggested that the Ni-OMD catalyst provides a better DMF yield in aqueous medium than any reported catalyst system.

### 3.5. Catalyst performance with various reaction parameters and metal–support interfacial interactions

The catalytic performance of the Ni-OMD catalyst with respect to reaction temperature is shown in Fig. 7a and schematic pathway for

hydrogenation is shown in Scheme 1. A gradual increase in HMF conversion has noticed with the increase in reaction temperature, and at 200 °C the conversion reaches ~100%. The selectivity to DMF also followed the same trend and achieved 99.5% at 150 °C. At room temperature 8.7% conversion of HMF to DMF was observed with 48.1% and 29.9% DHMF and MFA selectivity. With increasing temperature the rate of conversion to MFA to DMF was found to be very high in comparison with that of HMF to DHMF (Fig. 7a). The <sup>1</sup>H NMR pattern of the isolated compound is shown in Fig. S16 in the Supporting Information. H<sub>2</sub> pressure (Fig. 7b) shows no such noticeable effect on hydro-deoxygenation of HMF. The conversion to HMF steadily increased with H<sub>2</sub> pressure and ~100% HMF conversion was achieved at 3 MPa; ≥99% DMF selectivity was observed even at 2 MPa H<sub>2</sub> pressure.

To optimize the reaction conditions, we have run the reaction to a prolonged time with regular withdrawal of product; the data are

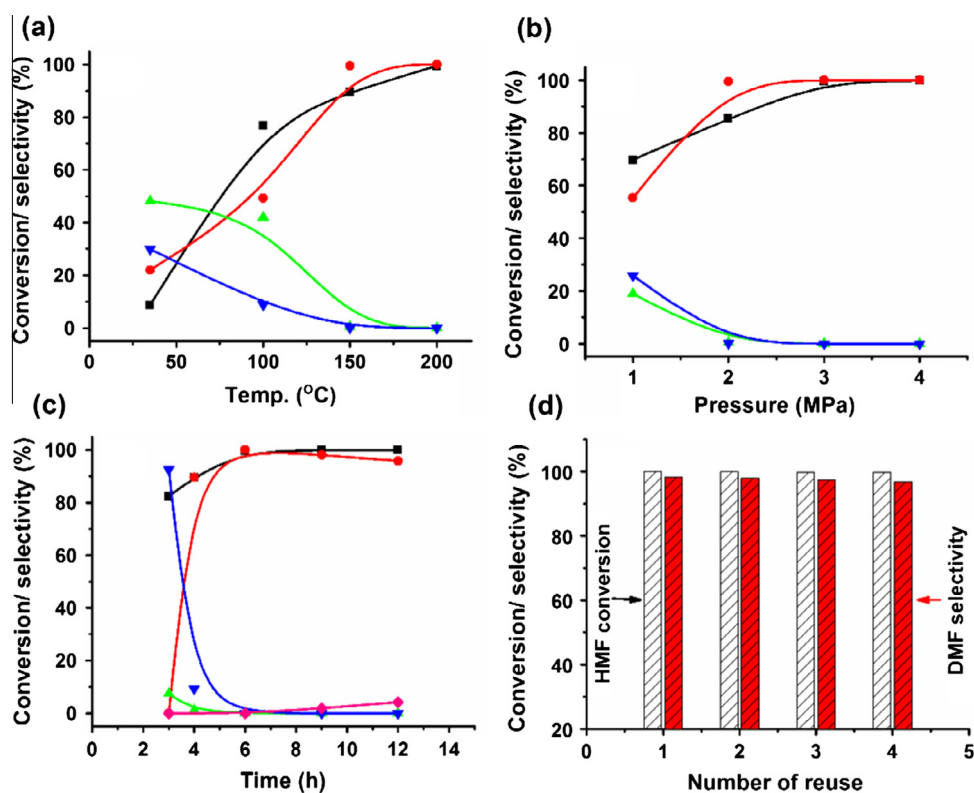


Fig. 7. (a) Effect of reaction temperature, (b) pressure, (c) time on stream, and (d) catalyst reusability for the hydro-deoxygenation of HMF. [■] conversion of HMF, [●] selectivity to DMF, [▲] selectivity to DHMF, and [▼] selectivity to MFA. Conditions: (general) 20 ml of 0.1 M HMF solution in H<sub>2</sub>O, 0.05 g reduced catalyst, temperature 200 °C, H<sub>2</sub> 30 bar, reaction time 6 h.

shown in Fig. 7c. It can be observed that the HMF conversion reaches ~100% after 6 h of reaction, whereas, DMF selectivity took a huge shift from 0% to 98.7% after 6 h of reaction. To elucidate the effect of nickel loading, catalysts with different (1–5%) nickel loadings were prepared. It was observed that with 1% nickel loading, the conversion to HMF reaches 74.8% but the main products obtained are DMF with 99.5% selectivity (Table 3). On the other hand, with increasing nickel loading up to 5%, the conversion to HMF is 100% with a little decrease in selectivity toward DMF (96.2%).

As seen from Tables 1 and 3, Ni nanoparticles of <5 nm size on mesoporous CN<sub>x</sub> (Ni-OMD3) clearly exhibit higher activity than the corresponding catalysts prepared by the citric acid reduction method, despite the fact that the same metal loading was used and the BET surface areas for the two forms were still comparable to each other (~535–490 m<sup>2</sup> g<sup>-1</sup>). A higher dispersion of Ni achieved on the CN<sub>x</sub> material by the organic matrix deposition method due to enhancement of the interfacial interactions between the Ni precursor and the support could be a reason for this observation. It is noted that when Ni loading increased from 1% to 5% the selectivity toward DMF decreased with constant increase to HMF conversion compared with the lower loading catalyst prepared using organic matrix deposition. As a result, the DMF yield of 3% Ni on CN<sub>x</sub> reaches nearly 100%, indicative of the remarkable activity dependence on the metal–support synergy. Additionally, higher loading of Ni causes an increase in mean particle size (as shown in Table 3); hence it can be concluded that Ni particles <5 nm facilitate the hydrogenation reaction. This observation proves that synergy between Ni nanoparticles and mesoporous CN<sub>x</sub> plays a crucial role in the high activity, and the organic matrix deposition method not only stops coalescence and agglomeration of the Ni nanoparticles but also increases the Ni dispersion and concentration of the catalyst.

The reusability of the catalyst was tested by conducting four successive runs with the same catalyst. The catalyst was recovered at different finite conversion levels, dried overnight, and reduced before the reaction at 700 °C. The catalyst showed similar hydrogenation activity but a negligible (only 2%) drop in DMF selectivity was seen (Fig. 7d and Table S2 in the Supplementary Information).

### 3.6. Role of catalyst support

We have also studied the role of the catalyst support, MCN<sub>x</sub>. We found that the support stabilizes the Ni atoms and small clusters of nickel atoms. We observed that mono-, di-, and triatomic metal clusters may fit into the cavity of the support without distorting the structure of the support (Fig. S17 in the Supplementary Information). We also found that for these three clusters, absorption free energies are negative. For bigger clusters, absorption energies may be negative, but they should absorb onto the surface of the support, not in the cavity of the support.

We have computed the activation energies for transition state 1 (detailed below), taking mono-, di-, and triatomic clusters of nickel absorbed on a catalyst support. Computed results are presented in

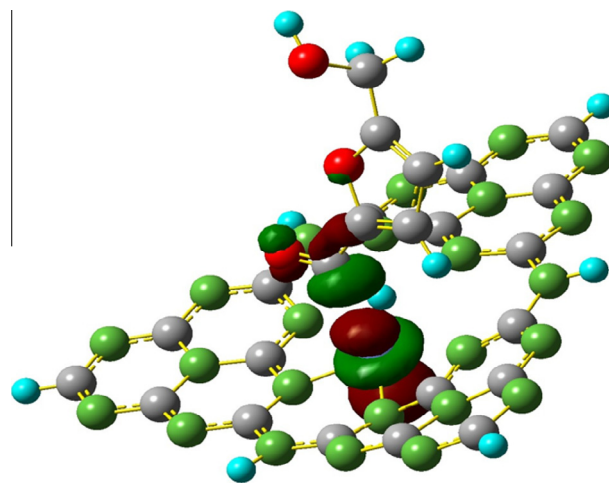


Fig. 8. Orbital picture of HOMO of TS-1 using mononickel cluster on MCN<sub>x</sub> support.

Table S3 in the Supporting Information. From Table S3, it is observed that the activation energy for TS-1 when the nickel catalyst is placed on the MCN<sub>x</sub> support increases for mono- and dinickel clusters but decreases for trinickel clusters. In all three cases, activation energies are higher than that calculated without a support, which is 6.26 kcal/mol. Thus, it seems that addition of support deactivates the catalyst. But if we consider the absorption energies, which are negative in all three cases, we found that addition of the support energetically favored the catalysis. Optimized geometries of transition states for mono-, di-, and trinickel clusters using MCN<sub>x</sub> support are presented in Fig. S18 and an orbital picture of HOMO of TS-1 for mononickel catalyst on support is given in Fig. 8, which shows that the use of a support does not disturb  $\sigma$ -bond formation by the Ni catalyst with the C-4 carbon of the reactant.

### 3.7. Mechanistic study

#### 3.7.1. Center of hydrogenation

In the applied method for calculations, the first step is hydrogenation of the aldehyde carbon of HMF. There are three distinct centers of HMF where hydrogenation may take place, C=O, C=C, and C–O; nevertheless, hydrogenation takes place at the aldehyde carbon faster than at the other two functional groups. To understand why the aldehyde carbon reacts faster than the others, DFT studies have been performed. For the studied catalyst system, Ni-MNC<sub>x</sub>, hydrogenation occurs through electrophilic substitution. We have studied the electrophilicity of different carbon atoms and oxygen atoms present in the HMF molecule using the condensed Fukui function [54,55]. We have also calculated the relative electrophilicity of these atoms [56,57]. For both these calculations we used Mulliken charges [58] with the charge of hydrogen atoms summed into that of heavy atoms to which they are connected. We

Table 3  
Effect of Ni particle size on catalytic activity.

Entry	Catalyst	Particle size <sup>a</sup>	Loading of Ni [wt.%] <sup>b</sup>	Conversion (mol.%)	Selectivity (mol.%) <sup>c</sup>	$\Phi_f^d$
1	Ni-OMD1	1.92	1	74.8	99.5	4.4
2	Ni-OMD3	3–3.5	3	>99.9	99.7	1.9
3	Ni-OMD5	6.8–10.8	5	100	96.2	1.1

<sup>a</sup> Mean particle diameter (in nm) calculate from HRTEM (except Ni-OMD1, which was calculated by the Scherer equation for the XRD data of the reduced catalyst).

<sup>b</sup> From the ICP study.

<sup>c</sup> Selectivity to DMF.

<sup>d</sup>  $\Phi_f$  = rate of formation  $\times 10^3$ .

observe that C-4, the aldehyde carbon, has the highest electrophilicity (0.177), and its electrophilicity is greater by a huge margin (0.06) than that of the second most electrophilic center (in Table S4, Supplementary Information), which is C-11, one of the C=C carbons (Fig. S19 in the Supplementary Information). The relative electrophilicity calculation also suggests that C-4 is the most electrophilic (1.878) center, which explains why hydrogenation proceeds faster for C=O than for other possible centers.

From the electron cloud distribution of the transition state of the hydrogenation process, a similar conclusion may be drawn. In Fig. 9, the electron cloud distribution of transition state 1 of hydrogenation is presented. Fig. 9a shows the distribution of the electron cloud of C=C, Fig. 9b represents the  $d-z^2$  orbital electron cloud of Ni, i.e., a lone pair of Ni atoms (catalyst of this reaction), and Fig. 9c represents the electron cloud of the C-4 atom and the  $d-z^2$  orbital of the Ni atom. From these distribution patterns it is clear that the electron cloud orientation of C=C does not match the electron cloud of the lone pair of the Ni atom for either  $\sigma$ -bond or  $\pi$ -bond formation. On the other hand, the electron cloud distribution of the C-4 atom matches the electron cloud distribution of the lone pair of the Ni atom for  $\sigma$ -bond formation (Fig. 9c). Thus, the C-4 atom is suitable for hydrogenation by the Ni atom.

### 3.7.2. Reaction pathways for hydrogenation

The hydrogenation reaction of HMF to DMF over highly dispersed nickel particles may occur in two different ways: either by abstraction of hydrogen by the carbonyl carbon atom (path 1

in Fig. 10), or by abstraction of hydrogen by the carbonyl oxygen atom (path 2 in Fig. 10) first followed by hydrogenolysis of CH<sub>2</sub>OH to a methyl group. From electrophilicity calculation, we have found that path 1 is favorable. The activation energies of these two proposed mechanisms have also been calculated. The activation energy of path 1 is 0.271 eV (6.26 kcal/mol), which is much lower than the activation energy of path 2, 2.597 eV. The relative stability of the intermediates also favors path 1, as intermediate 1 involves a negative charge on the carbonyl oxygen atom, which is more stable than the negative charge on carbonyl carbon formed in path 2.

In addition, we have extended our study by including the catalyst support interaction for path 1; the transition state 1 with catalyst support is shown in Fig. 11. The activation energy for this process is 2.126 eV (49.02 kcal/mol), which is significantly higher than that calculated without catalyst support (0.271 eV or 6.26 kcal/mol), but at the same time the absorption energy of a single Ni atom in the cavity of the support is  $-4.118$  eV or  $-94.96$  kcal/mol. Thus, the high activation energy of path 1 is overcome by the absorption energy and the overall energy for these two process is  $-45.94$  kcal/mol. Thus, in the presence of a support we get negative free energy for path 1, which eases the catalytic process.

### 3.7.3. Hydrogenolysis

After hydrogenation of HMF, a dihydroxy intermediate (DHMF) is formed, which on hydrogenolysis yields DMF. The intermediate has two different types of oxygen atoms; ring oxygen and hydroxyl oxygens. Only the hydrogenolysis of hydroxyl oxygen yields our target compound. To understand the priority of hydrogenolysis, we

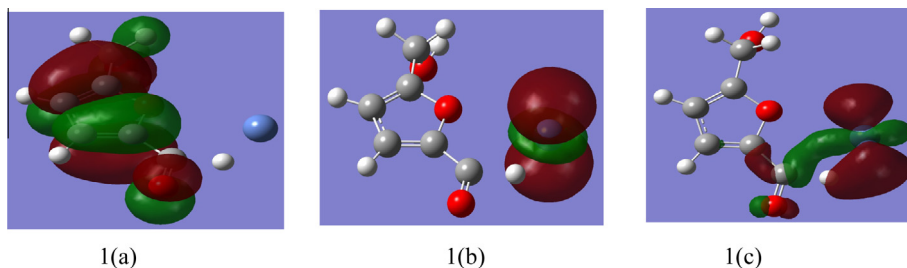


Fig. 9. Electron cloud distribution of transition state 1 (TS-1) of the hydrogenation process.

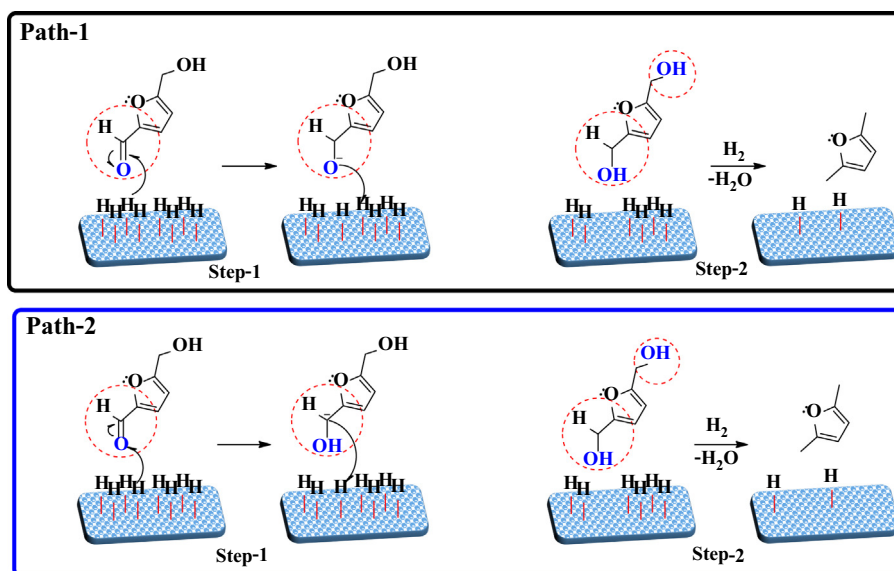


Fig. 10. Probable reaction pathways.

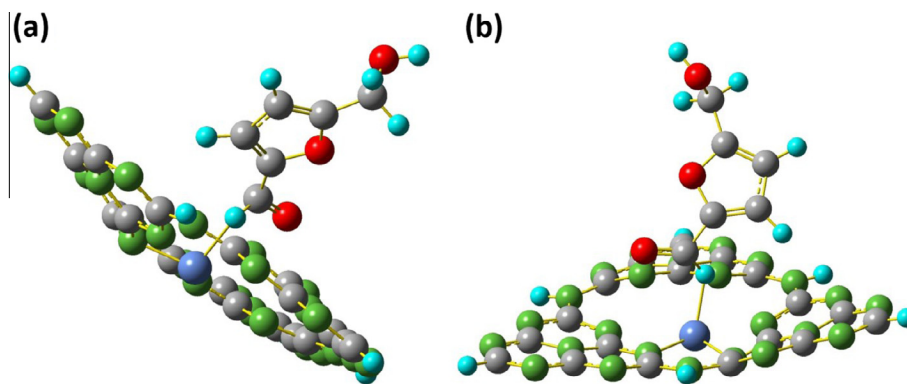


Fig. 11. Transition state 1 (TS-1) of the hydrogenation process via path 1.

calculate the electrophilicity of oxygen atoms. We find that ring oxygen (O1) has the lowest electrophilicity (0.044) compared with two hydroxyl oxygens (0.059 and 0.116 for O9 and O15, respectively). Electrophilicity values of the three oxygen atoms clearly suggest that hydrogenolysis will take place at O15 first and then O9. The probability of hydrogenolysis of the ring oxygen is very low.

#### 4. Conclusions

Several methodologies have been applied to develop highly dispersive Ni catalysts for selective hydrogenation of HMF to DMF on a mesoporous nitrogen-rich carbon support. Among all the studied catalyst systems, the organic matrix deposition method is found to be more promising for synthesis of highly dispersed supported nickel catalysts (up to 46.2%), which makes the catalyst a good to excellent noble-metal-free catalyst system compared with other catalyst systems for selective HMF hydrogenation.

The promoting effect of the catalyst system can be attributed to the strong metal–support interfacial interaction. This metal–support synergy between the nitrogen atoms of the support material and Ni nanoparticle can be achieved only with very small (below 5 nm) Ni nanoparticles, which are highly dispersed on the support. When particle size is above 5 nm, DMF selectivity goes down, and the same can be observed for Ni dispersion. The strong interaction between Ni and nitrogen atoms of the support enhances the total Ni reduction and hence increases the overall hydrogenation activity of the catalyst system (more than 99.9% conversion with 98.7% DMF selectivity).

From theoretical studies it has been observed that the aldehyde carbon has the highest electrophilicity (0.177), greater by a huge margin (0.06) than the second most electrophilic center, one of the C=C carbons. The relative electrophilicity calculation also suggests that the aldehyde carbon is the most electrophilic (1.878) center; this explains why the hydrogenation proceeds faster through C=O than through other possible centers. In addition, the mechanistic pathway for HMF hydrogenation over the Ni-OMD3 catalyst was evaluated, which provides conceptual insight into for HFM conversion over a heterogeneous Ni-supported mesoporous nitrogen-rich carbon catalyst.

Detailed characterization techniques, low-angle XRD, N<sub>2</sub> adsorption–desorption isotherm, HR-TEM, XPS, and TPR of different Ni-CA and Ni-OMD are available at <http://dx.doi.org/10.1016/j.jcat.2016.05.012>.

#### Acknowledgments

We are thankful to DST, New Delhi for financial support in the form of an AISRF-GC grant. R.G. and N.S acknowledge the Council

for Scientific and Industrial Research (CSIR), India. We also acknowledge the Director of CSIR-IIP for his support. The authors thank Analytical Science Division, Indian Institute of Petroleum for analytical services.

#### Appendix A. Supplementary material

Supplementary data associated with this article can be found, in the online version, at <http://dx.doi.org/10.1016/j.jcat.2016.05.012>.

#### References

- [1] P.C.A. Bruijninx, Y.R.S. Leshkov, *Catal. Sci. Technol.* 4 (2014) 2180–2181.
- [2] J.M. Tour, C. Kittrell, V.L. Colvin, *Nat. Mater.* 9 (2010) 871–874.
- [3] J.C. Colmenares, R. Luque, *Chem. Soc. Rev.* 43 (2014) 765–778.
- [4] L. Hu, L. Lin, S. Liu, *Ind. Eng. Chem. Res.* 53 (2014) 9969–9978.
- [5] M. Mascal, E.B. Nikitin, *Angew. Chem. Int. Ed.* 47 (2008) 7924–7926.
- [6] B. Saha, C.M. Bohn, A. Omar, *ChemSusChem* 7 (2014) 3095–3101.
- [7] D.M. Alonso, J.Q. Bond, J.A. Dumesic, *Green Chem.* 12 (2010) 1493–1513.
- [8] J.B. Binder, R.T. Raines, *J. Am. Chem. Soc.* 131 (2009) 1979–1985.
- [9] M.J. Climent, A. Corma, S. Iborra, *Green Chem.* 16 (2014) 516–547.
- [10] J. Chen, R. Liu, Y. Guo, L. Chen, H. Gao, *ACS Catal.* 5 (2015) 722–733.
- [11] R.J. Van Putten, J.C. Van der Waal, E.D. Jong, C.B. Rasrendra, H.J. Heeres, J.G. de Vries, *Chem. Rev.* 113 (2013) 1499–1597.
- [12] D. Scholz, C. Aellig, I. Hermans, *ChemSusChem* 7 (2014) 268–275.
- [13] A.K. Agarwal, *Prog. Energy Combust. Sci.* 33 (2007) 233–271.
- [14] Y. Qian, L. Zhu, Y. Wang, X. Lu, *Renew. Sustain. Energy Rev.* 41 (2015) 633–646.
- [15] Y.B. Huang, M.Y. Chen, L. Yan, Q.X. Guo, Y. Fu, *ChemSusChem* 7 (2014) 1068–1070.
- [16] Y.R. Leshkov, C.J. Barrett, Z.Y. Liu, J.A. Dumesic, *Nature* 447 (2007) 982–985.
- [17] G.H. Wang, J. Hilgert, F.H. Richter, F. Wang, H.J. Bongard, B. Splietho, C. Weidenthaler, F. Schüth, *Nat. Mater.* 13 (2014) 293–300.
- [18] P. Nilges, U. Schroder, *Energy Environ. Sci.* 6 (2013) 2925–2931.
- [19] E. Martono, J.M. Vohs, *J. Catal.* 291 (2012) 79–86.
- [20] R.J. White, R. Luque, V.L. Budarin, J.H. Clark, D.J. Macquarrie, *Chem. Soc. Rev.* 38 (2009) 481–494.
- [21] J.Q. Bond, D.M. Alonso, D. Wang, R.M. West, J.A. Dumesic, *Science* 327 (2010) 1110–1114.
- [22] B.X. Peng, X.G. Yuan, C. Zhao, J.A. Lercher, *J. Am. Chem. Soc.* 134 (2012) 9400–9405.
- [23] D.I. Enache, J.K. Edwards, P. Landon, B. Solsona-Espriu, A.F. Carley, A.A. Herzing, M. Watanabe, C.J. Ckiely, D.W. Knight, G.J. Hutchings, *Science* 311 (2006) 362–365.
- [24] X. Kong, R. Zheng, Y. Zhu, G. Ding, Y. Zhu, Y.W. Li, *Green Chem.* 17 (2015) 2504–2514.
- [25] R. Goyal, B. Sarkar, N. Lucas, A. Bordoloi, *ChemCatChem* 6 (2014) 3091–3109.
- [26] V.Z. Radkevich, T.L. Senko, K. Wilson, L.M. Grishenko, A.N. Zaderko, V.Y. Diyuk, *Appl. Catal. A* 335 (2008) 241–251.
- [27] S.B. Yang, X.L. Feng, X.C. Wang, K. Mullen, *Angew. Chem. Int. Ed.* 50 (2011) 5339–5343.
- [28] X. Xu, Y. Li, Y. Gong, P. Zhang, H. Li, Y. Wang, *J. Am. Chem. Soc.* 134 (2012) 16987–16990.
- [29] B. Sarkar, C. Pendem, L.N.S. Konathala, T. Sasaki, R. Bal, *J. Mater. Chem. A* 2 (2014) 18398–18404.
- [30] P. Karandikar, K.R. Patil, A. Mitra, B. Kakade, A.J. Chandwadkar, *Micropor. Mesopor. Mat.* 98 (2007) 189–199.
- [31] P. Hohenberg, W. Kohn, *Phys. Rev.* 136 (1964) 864–871.
- [32] Gaussian 09, Revision D.01, M.J. Frisch, G.W. Trucks, B.H. Schlegel, G.E. Scuseria, M.A. Robb, J.R. Cheeseman, G. Scalmani, V. Barone, B. Mennucci, G.A. Petersson, H. Nakatsuji, M. Caricato, X. Li, P.H. Hratchian, A.F. Izmaylov, J.

- Bloino, G. Zheng, J.L. Sonnenberg, M. Hada, M. Ehara, K. Toyota, R. Fukuda, J. Hasegawa, M. Ishida, T. Nakajima, Y. Honda, O. Kitao, H. Nakai, T. Vreven, J.A. Montgomery, J.E. Peralta Jr., F. Ogliaro, M. Bearpark, J.J. Heyd, E. Brothers, K.N. Kudin, V.N. Staroverov, R. Kobayashi, J. Normand, K. Raghavachari, A. Rendell, J. C. Burant, S.S. Iyengar, J. Tomasi, M. Cossi, N. Rega, J.M. Millam, M. Klene, J.E. Knox, J.B. Cross, V. Bakken, C. Adamo, J. Jaramillo, R. Gomperts, R.E. Stratmann, O. Yazyev, A.J. Austin, R. Cammi, C. Pomelli, J.W. Ochterski, R.L. Martin, K. Morokuma, V.G. Zakrzewski, G.A. Voth, P. Salvador, J.J. Dannenberg, S. Dapprich, A.D. Daniels, O. Farkas, J.B. Foresman, J.V. Ortiz, J. Cioslowski, D.J. Fox, Gaussian, Inc., Wallingford CT, 2009.
- [33] A.D. Becke, *Phys. Rev. A* 38 (1988) 3098–3100.
- [34] J.P. Perdew, in: P. Ziesche, H. Eschrig (Eds.), *Electronic Structure of Solids '91*, Akademie Verlag, Berlin, 1991, p. 11.
- [35] J.P. Perdew, J.A. Chevary, S.H. Vosko, K.A. Jackson, M.R. Pederson, D.J. Singh, C. Fiolhais, *Phys. Rev. B* 46 (1992) 6671–6687.
- [36] J.P. Perdew, J.A. Chevary, S.H. Vosko, K.A. Jackson, M.R. Pederson, D.J. Singh, C. Fiolhais, *Phys. Rev. B* 48 (1993) 6671–6687.
- [37] J.P. Perdew, K. Burke, Y. Wang, *Phys. Rev. B* 54 (1996) 16533–16539.
- [38] L.E. Roy, P.J. Hay, R.L.J. Martin, *Chem. Theor. Comput.* 4 (2008) 1029–1031.
- [39] J. Geng, D.A. Jefferson, B.F.G. Johnson, *Chem. Commun.* 9 (2007) 969–971.
- [40] N. Fairley, Casa XPS Version 2.3.15, Copyright 1999–2009 Casa Software Ltd.
- [41] C.D. Wagner, W.M. Riggs, L.E. Davis, J.F. Moulder, G.E. Muilenberg, *Handbook of X-ray Photoelectron Spectroscopy*, PerkinElmer Corp., Eden Prairie, USA, 1979.
- [42] S.I. Tanase, D. Tanase, D. Dobromir, A.V. Sandu, V.J. Georgescu, *Superconduct. Nov. Magn.* 28 (2015) 1–7.
- [43] R. Goyal, D. Dumbre, M. Pandey, L.N.S. Konthala, A. Bordoloi, *Catal. Sci. Technol.* 5 (2015) 3632–3638.
- [44] H.W. Nesbitt, D. Legrand, G.M. Bancroft, *Phys. Chem. Miner.* 27 (2000) 357–366.
- [45] H.E.B. Lempers, R.A. Sheldon, *J. Catal.* 175 (1998) 62–69.
- [46] W.S. Leong, C.T. Nai, J.T.L. Thong, *Nano Lett.* 14 (2014) 3840–3847.
- [47] V.M. Dhavale, S.S. Gaikwad, L. George, R.N. Devi, S. Kurungot, *Nanoscale* 6 (2014) 13179–13187.
- [48] R. Wojcieszak, M. Zieliński, S. Monteverdi, M.M. Bettahar, *J. Colloid Interf. Sci.* 299 (2006) 238–248.
- [49] S.B. Wang, G.Q. Lu, *Carbon* 36 (1998) 283–292.
- [50] M.C.R. Martínez, D.C. Amorós, A.L. Solano, C.S. Martínez, D. Lecea, H. Yamashita, M. Anpo, *Carbon* 33 (1995) 3–13.
- [51] J. Jae, W. Zheng, R.F.D.G. Vlachos, *ChemSusChem* 6 (2013) 1158–1161.
- [52] T. Thananathanachon, T.B. Rauchfuss, *Angew. Chem. Int. Ed.* 49 (2010) 6616–6618.
- [53] J. Zhang, C. Chen, W. Yan, F. Duan, B. Zhang, Z. Gao, Y. Qin, *Catal. Sci. Technol.* 6 (2016) 2112–2119.
- [54] W. Langenaeker, M. De Decker, P. Geerlings, P.J. Raeymaekers, *Mol. Struct. Theochem.* 207 (1990) 115–130.
- [55] S. Arulmozhiraja, P. Kolandaivel, *Mol. Phys.* 90 (1997) 55–62.
- [56] R.K. Roy, S. Krishnamurti, P. Geerlings, S. Pal, *J. Phys. Chem. A* 102 (1998) 3746–3755.
- [57] R.K. Roy, F. De Proft, P. Geerlings, *J. Phys. Chem. A* 102 (1998) 7035–7040.
- [58] R.S. Mulliken, *J. Chem. Phys.* 23 (1955) 1833–1840.